Silicate clouds and a circumplanetary disk in the YSES-1 exoplanet system

https://doi.org/10.1038/s41586-025-09174-w

Received: 3 September 2024

Accepted: 20 May 2025

K. K. W. Hoch[1✉], M. Rowland[2], S. Petrus[3,4,5], E. Nasedkin[6,7], C. Ingebretsen[8], J. Kammerer[9], M. Perrin[1], V. D'Orazi[10,24], W. O. Balmer[8], T. Barman[11], M. Bonnefoy[12], G. Chauvin[6], C. Chen[1], R. J. De Rosa[13], J. Girard[1], E. Gonzales[14], M. Kenworthy[15], Q. M. Konopacky[16], B. Macintosh[17,18], S. E. Moran[3,11], C. V. Morley[2], P. Palma-Bifani[19,20], L. Pueyo[1], B. Ren[19], E. Rickman[21], J.-B. Ruffio[16], C. A. Theissen[16], K. Ward-Duong[22] & Y. Zhang[23]

Young exoplanets provide an important link between understanding planet formation and atmospheric evolution[1]. Direct imaging spectroscopy allows us to infer the properties of young, wide-orbit, giant planets with high signal-to-noise ratio. This allows us to compare this young population with exoplanets characterized by transmission spectroscopy, which has indirectly revealed the presence of clouds[2–4], photochemistry[5] and a diversity of atmospheric compositions[6,7]. Direct detections have also been made for brown dwarfs[8,9], but direct studies of young giant planets in the mid-infrared were not possible before James Webb Space Telescope[10]. With two exoplanets around a solar-type star, the YSES-1 system is an ideal laboratory for studying this early phase of exoplanet evolution. Here we report the direct observations of silicate clouds in the atmosphere of the exoplanet YSES-1 c through its 9–11 μm absorption feature, and the first circumplanetary disk silicate emission around its sibling planet, YSES-1 b. The clouds of YSES-1 c are composed of either amorphous iron-enriched pyroxene or a combination of amorphous $MgSiO_3$ and Mg_2SiO_4, with particle sizes of ≤0.1 μm at 1 millibar pressure. We attribute the emission from the disk around YSES-1 b to be from submicron olivine dust grains, which may have formed through collisions of planet-forming bodies in the disk.

The YSES-1 (TYC 8998-760-1, 2MASS J13251211-6456207) system consists of two Jovian planets around a young, solar mass star. Located at 94 parsec in the Sco-Cen star-forming region[11–13], these widely separated planets at about 160 AU and 320 AU projected separation (1.6 arcsec and 3.2 arcsec angular distance) exhibit favourable contrast (3×10^{-3} and 1×10^{-4} in K-band), providing an ideal laboratory for spectroscopic reconnaissance of a low mass ratio (0.005) exoplanetary system. The estimated masses are $14 \pm 3 M_{\rm Jup}$ and $6 \pm 1 M_{\rm Jup}$ based on evolutionary models for the 16.7 ± 1.4 Myr system age[11]. Located near the L/T transition, both planets are much redder than other exoplanets and field brown dwarfs[11], suggesting that they have distinct atmospheric conditions or processes. At near-infrared (NIR) wavelengths, YSES-1 b is accessible using ground-based spectroscopy, whereas YSES-1 c is too faint for such measurements. K-band (about 2.5 μm) spectroscopy of YSES-1 b revealed molecular features from H_2O, CO and the direct $^{12}CO/^{13}CO$ isotope ratio measurement. Moreover, observations of Hα line emission from YSES-1 b indicate gas accretion onto the planet, implying the ongoing formation of this system[14,15].

We present new James Webb Space Telescope (JWST) observations of YSES-1 b and c, consisting of low-resolution ($R \sim 100$) spectra from 0.6 μm to 12 μm (Fig. 1). Both planets are visible in the raw data without any need for starlight suppression (see Methods for details of observations and data processing). The spectra for both planets show clear signatures of CO, H_2O, CO_2 and CH_4 from 1 μm to 5 μm, and H_2O absorption from 5 μm to 7 μm. Notably, for the outer planet YSES-1 c, the absorption feature seen from 9 μm to 12 μm is consistent with silicate clouds (Fig. 1). As a late-L (about L7.5)-type object, YSES-1 c is expected to have silicate clouds, similar to other mid- to late-L-type brown dwarfs[16–19], although the shape of its silicate feature is distinct from that of comparable objects (Fig. 2).

To characterize the physical and atmospheric parameters for each planet, we conduct two independent analyses, using ForMoSA[20,21] coupled with the Exo-Rem[22] grid to forward model the spectra and

---

[1]Space Telescope Science Institute, Baltimore, MD, USA. [2]The University of Texas at Austin, Austin, TX, USA. [3]NASA-Goddard Space Flight Center, Greenbelt, MD, USA. [4]Instituto de Estudios Astrofísicos, Facultad de Ingeniería y Ciencias, Diego Portales University, Santiago, Chile. [5]Millennium Nucleus on Young Exoplanets and their Moons (YEMS), Santiago, Chile. [6]Max-Planck-Institut für Astronomie, Heidelberg, Germany. [7]Trinity College Dublin, The University of Dublin, Dublin, Ireland. [8]Johns Hopkins University, Baltimore, MD, USA. [9]European Southern Observatory, Garching, Germany. [10]INAF - Padova Astronomical Observatory, Padova, Italy. [11]Lunar and Planetary Laboratory, University of Arizona, Tucson, AZ, USA. [12]University of Grenoble Alpes, Saint-Martin-d'Hères, France. [13]European Southern Observatory, Alonso de Córdova, Vitacura, Chile. [14]San Francisco State University, San Francisco, CA, USA. [15]Leiden Observatory, Leiden University, Leiden, The Netherlands. [16]UC San Diego, La Jolla, CA, USA. [17]University of California Observatories, Santa Cruz, CA, USA. [18]University of California Santa Cruz, Santa Cruz, CA, USA. [19]Observatoire de la Cote d'Azur, Nice, France. [20]LESIA, Observatoire de Paris, Université Paris Sciences et Lettres, CNRS, Sorbonne University, Université de Paris, Paris, France. [21]European Space Agency Office, European Space Agency, Space Telescope Science Institute, Baltimore, MD, USA. [22]Smith College, Northampton, MA, USA. [23]California Institute of Technology, Pasadena, CA, USA. [24]Present address: The University of Texas at Austin, Austin, TX, USA. ✉e-mail: khoch@stsci.edu

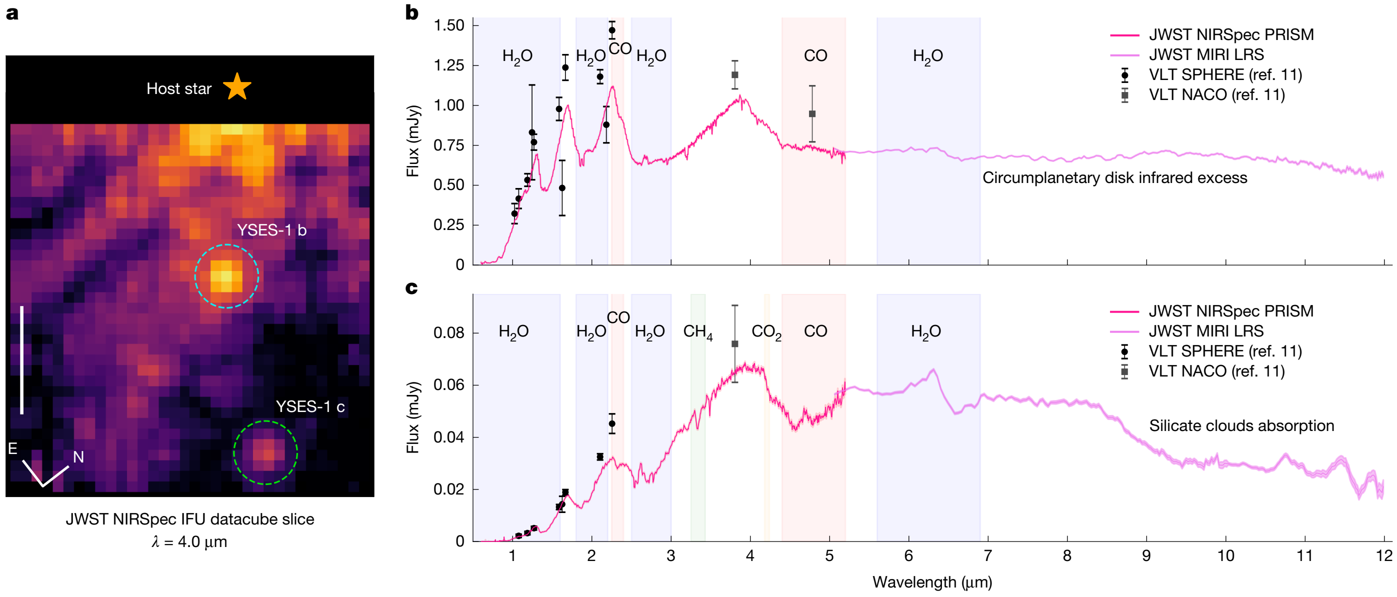

Fig. 1 | Observed spectra of YSES-1 b and c. a, A single wavelength (4 µm) slice from the NIRSpec IFU prism datacube, showing the geometry of the system. Both planets can be directly seen as point sources within the square instrumental field of view, along with a point spread function (PSF) halo of glare from the host star, which was located just outside of the IFU entrance aperture, as indicated. This PSF halo was modelled and subtracted in data analyses before spectral extraction for the planets. **b**,**c**, The observed spectra of YSES-1 b (**b**) and YSES-1 c (**c**). Solid lines show the spectra measured with JWST NIRSpec and MIRI; shaded regions on either side of the line indicate the 1σ measurements uncertainties, but these are generally small, comparable to the thickness of the line. Symbols indicate previous ground-based photometric measurements from the literature, also with 1σ uncertainties. The coloured bands label the major molecular and continuum components. Scale bar, 1 arcsec, 94 AU (**a**).

petitRADTRANS (pRT)[23] to perform atmospheric retrievals (Methods). With high signal-to-noise ratio (SNR) and broad wavelength coverage, both methods can infer precise measurements of physical parameters. However, the dominant source of uncertainty is the systematics in the models, which are not reflected in the measured posterior distributions[24]. For completeness, we present the statistical uncertainties associated with each model in Extended Data Table 3, although we adopt preferred parameter ranges spanning the measurements from each method to reflect the model uncertainty.

Beginning with YSES-1 c, we find that no existing grid of cloudy, self-consistent atmospheric models (for example, Exo-Rem[25]) reproduces the silicate feature of YSES-1 c. Based on the combined forward modelling and retrieval analysis, we find an effective temperature range of 950–1,100 K and a surface gravity range of 3.0–3.7 dex. From a composition standpoint, our analyses yield a metallicity ([M/H]) range of 0.27–0.52 and an atmospheric carbon-to-oxygen (C/O) ratio of 0.60–0.72. Up to 18% of oxygen can be sequestered in the silicate clouds in brown dwarfs[22], which assumes 3.28 oxygen atoms per silicon atom condensing in $MgSiO_3$ and Mg_2SiO_4 (ref. 26). Accounting for this, the resultant bulk C/O ratio from the atmospheric retrievals is 0.65. Overall, the ForMoSA analysis indicates solar composition for the atmosphere of YSES-1 c, whereas the pRT retrieval hints at modestly enriched abundances, comparable to other directly imaged exoplanets[27].

Late L-type field brown dwarfs[8] and companions such as VHS 1256 b (ref. 9) share similar deep silicate absorption features in the mid-infrared region. In comparison, YSES-1 c has a unique silicate absorption feature as shown in Fig. 2a,b. The absorption begins at longer wavelengths compared with those objects closer to 8.5 µm rather than 7.5–7.8 µm for the brown dwarfs or 8.0 µm for VHS 1256 b. The shape and depth of the feature are also distinct. Using the cloudless atmosphere grid ATMO[28], we measure the silicate equivalent width indices[24] (Supplementary Information). We find that YSES-1 c has a large silicate index (Fig. 2c), following the trend of stronger and redder features for lower mass and younger objects. The depth of the feature is consistent with YSES-1 c sharing an equator-on inclination with its host (81° ± 9°; refs. 29,30), in which the cloud absorption strength is expected to be maximized[8]. This confirms that silicate clouds in young and low surface gravity objects are different from field-age free-floating brown dwarfs and substellar companions, previously proposed based on exoplanet colours[31] and silicate indices[8].

We explore the physical mechanisms underlying this difference by generating a suite of custom cloud models that include a variety of silicate species and fit them to the data longwards of 7 µm. We assume atmospheric properties based on our reported ranges and vary the cloud composition, mean grain size of the particles and cloud height in the atmosphere. We prioritize fitting the first half of the feature from 8.5 µm to 10 µm, for which the SNR is higher than at longer wavelengths. We fit three amorphous SiO_2, $MgSiO_3$ and Mg_2SiO_4 compositions, as shown in Fig. 3. The best-fit grain size distribution was tightly centred on 0.1 µm and the best cloud location was at 1 millibar of pressure for all cloud compositions tested. $MgSiO_3$ was the best fit, but a slight wavelength shift remained between the cloud model and the observed feature. We, therefore, fit additional pyroxene cloud models with differing fractions of iron (Fe) to shift the feature[32]. We also fit models that include two clouds with differing fractions of amorphous $MgSiO_3$ and Mg_2SiO_4. Finally, we fit models using the distribution of hollow spheres approximation, which redshifted the feature too far. Either a small amount of iron in the cloud particles or a combination consisting of 60–90% amorphous $MgSiO_3$ matches the data better than amorphous $MgSiO_3$ (see Fig. 3d and Extended Data Fig. 6 for further details of cloud modelling). These results are consistent with iron and magnesium hydrides condensing into thick clouds with smaller particles being lofted to low pressures[33]. Alternatively to silicate mixtures, it has recently been proposed that polymorphs of silica and other minerals may have a role in shifting cloud spectral features to longer wavelengths[34].

Independently, an atmospheric retrieval also finds that $MgSiO_3$ is the best-fit silicate for the clouds in YSES-1 c. We found that crystalline $MgSiO_3$ particles with a mean particle size of 0.20 ± 0.02 µm and a cloud base of 0.02 bar provided the best fit to the spectrum, broadly similar to the detailed modelling properties. An iron-enriched silicate cloud was also tested, with a composition of $Mg_{0.5}Fe_{0.5}SiO_3$ and was found to have a slightly worse χ^2/ν (9.86) than the pure enstatite cloud (7.18).

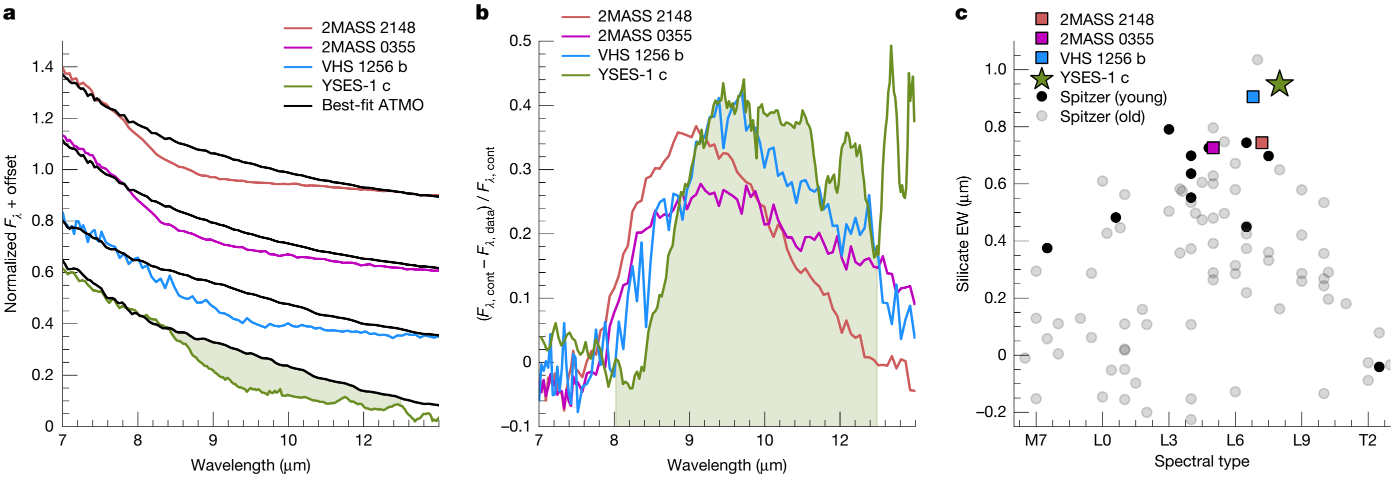

Fig. 2 | Semi-empirical analysis of the silicate absorption feature. The silicate feature of YSES-1 c is compared with the features seen in three examples of young substellar objects: VHS 1256 b, 2MASS 2148 and 2MASS 0355, ordered by decreasing mass. **a**, The observed spectra of each object (coloured lines) along with models for cloud-free atmospheres from the ATMO model grid (black lines). Note the shift towards longer wavelengths for the lower mass objects, particularly for YSES-1 c. **b**, The fractional reduction of emission at each wavelength because of the silicate clouds, computed as the flux ratio between the absorption depth and the cloud-free continuum model. The shaded region highlights the wavelength range used to calculate the silicate index. For clarity, this is shown only for YSES-1 c. However, the same range has been applied to all MIR spectra from JWST and the Spitzer library to ensure consistency in the analysis. **c**, Comparison of the silicate equivalent width (EW) indices of these objects and a broader sample of brown dwarfs from the Spitzer library. The two young substellar companions, YSES-1 c and VHS 1256 b, have among the highest silicate indices compared with the field sample.

For the iron-rich composition, the cloud base sinks to 0.4 bar and the particle size increases to 1.7 μm. The difference between the retrieved cloud structure and the detailed model probably stems from degeneracies between particle size and cloud base pressure that current cloud parameterizations cannot yet resolve. These degeneracies also exist between the cloud parameterization and the thermal profile[28], and we also find that the temperature profile of YSES-1 c follows a shallow temperature gradient, which also acts to redden the spectrum.

Although the atmosphere of YSES-1 b is too hot for silicates to condense into clouds, silicate emission from a circumplanetary dust disk (CPD) is visible in the Mid-Infrared Instrument (MIRI) observations. Previously detected Brackett-γ emission[14] indicates ongoing accretion onto the planet, hinting at the presence of circumplanetary material. Although high-contrast polarimetric observations were conducted to search for circumplanetary dust in this system[35], no disk signal was detected. Our JWST data reveal an infrared excess from 4 μm to 14 μm, confirming the presence of hot circumplanetary dust. This places YSES-1 b among the very few substellar companions around which circumplanetary disks are directly observed, including PDS 70 c (ref. 36) and GQ Lup B (ref. 37).

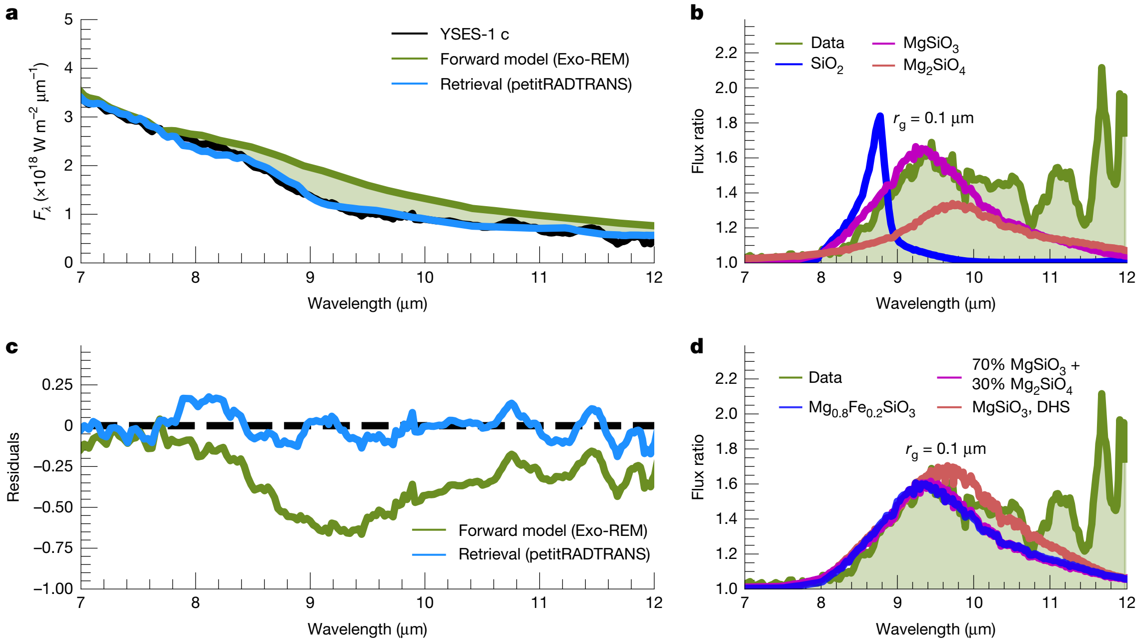

Fig. 3 | YSES-1 c spectral comparison against silicate cloud models. a,**b**, The spectrum of YSES-1 c centred on the silicate feature with the best-fit cloudy Exo-REM spectrum and best-fit retrieved spectrum (**a**), along with their residuals (**b**). **c**,**d**, The flux ratio between the best-fit Exo-REM model and the data (green) compared with the flux ratios between cloud-free models and cloud-free models with silicate clouds of different composition. All cloud models shown have a mean cloud particle radius of 0.1 μm and cloud base location of 1 millibar of pressure.

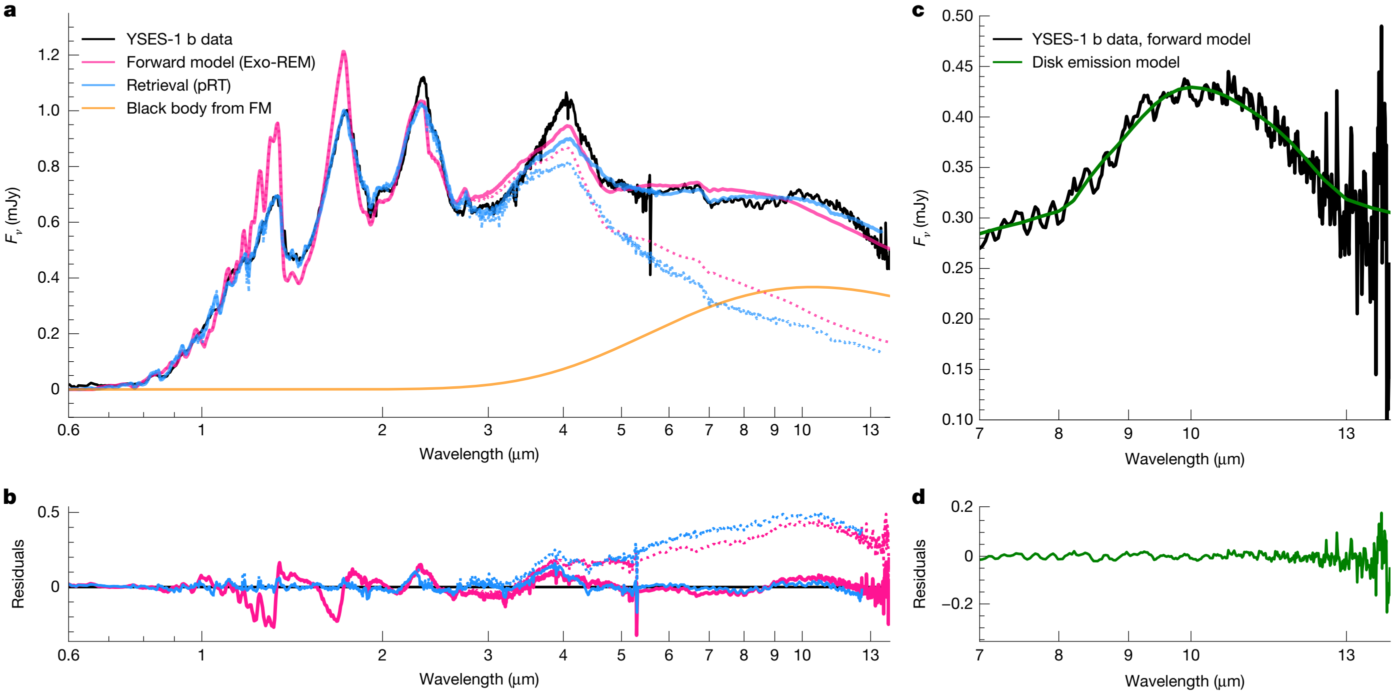

Fig. 4 | YSES-1 b spectral comparison against forward model, retrieval and thermal disk emission model. a,**b**, The spectrum of YSES-1 b is plotted in black against the best-fit cloudy Exo-REM spectrum with an added blackbody and without an added blackbody in pink, the best-fit petitRADTRANS retrieval with and without an added blackbody in blue, and the best-fit blackbody curve in orange (**a**) with residuals between the fits below (**b**). **c**,**d**, The best-fit thermal emission model is shown in green against the Exo-REM model without the added blackbody subtracted from the data divided by the error in the data in black.

We jointly fit atmospheric models for the planet atmosphere and circumplanetary disk thermal emission. We use the same forward modelling method from above, both with and without an additional blackbody to account for the CPD (see Fig. 4 and Methods, section 'Atmospheric forward modelling'). We find an effective temperature range of 1,600–2,020 K and surface gravity of 2.8–4.8 dex. The retrievals and forward models do not reproduce the spectra from about 1–2.5 µm, which is particularly sensitive to the surface gravity and metallicity[38]. This discrepancy may be because of the limited understanding of the impact of active accretion of material onto the atmospheres, as this has mostly been studied in protostars[39].

Both our forward models and retrievals find best-fit blackbody temperatures of about 500 K for the CPD, with a disk radius between 8.5–20R_{Jup}. This blackbody model cannot fully replicate the observed emission feature from 8–11 µm. The presence of this broad emission feature indicates the presence of µm-sized silicate grains in the CPD (Fig. 4b). This is the first clear detection of silicates in a CPD, in contrast to the blackbody appearance of the small sample of CPDs for which infrared spectra exist[37,40]. To quantify the dust properties, we apply physically motivated models that capture the thermal processing of dust grains in the CPD. We isolate the infrared excess by subtracting the planetary atmosphere continuum using the best-fit Exo-REM model. This infrared excess is fit with a disk emission model, assuming the material in the disk emits in thermal equilibrium, has a power law size distribution resulting from collisional equilibrium and is composed of olivine ($MgFeSiO_4$). This fit is shown in Fig. 4c. The emission is consistent with a disk of $MgFeSiO_4$ grains with a minimum size of 0.6 ± 0.04 µm and a temperature of 484.6 ± 7 K for the silicates and 602.1^{+36}_{-56} K for the blackbody component, corresponding to expected thermal equilibrium for dust 12–35R_{Jup} away from the planet. The estimated total dust mass for all particles smaller than 1 mm is about $1.1 \times 10^{-9} M_{\mathrm{Earth}}$ ($8.8 \times 10^{-8} M_{\mathrm{Moon}}$).

No other CPD has been found to have such small, hot grains to date[37]. The absence of small grains could be because of dust grains having already grown to sizes larger than 5 µm, which is seen in young systems[41,42]. For the protoplanetary disk of the Solar System, it is proposed that silicate grains experience thermal processing over time, for example, from colliding planetesimals, resulting in fine grain sizes. Given the age of the YSES-1 system, the presence of small, hot, olivine grains could indicate that we are seeing a later generation of thermally processed grains caused by collisions of larger satellite-forming material in the CPD[43,44].

Our analyses have shown both the complex atmospheric and environmental features of the YSES-1 system and the challenges in modelling the ongoing physical processes. We confirm the predicted presence of silicate clouds at high altitudes in YSES-1 c, establishing that these clouds are responsible for the extreme reddening of its spectrum. Identifying the detailed composition and structure of cloud particles is an important step in accounting for all oxygen sinks in an atmosphere. Measuring the cloud properties allows us to connect the atmospheric and bulk C/O, thus placing the planets in context with their host star (Supplementary Information). The circumplanetary material of YSES-1 b could be second-generation grains resulting from collisions of larger grains or the formation of moons, but a deeper understanding of the physics behind the emerging populations of CPDs is required. Future studies of silicate clouds and circumplanetary material will continue to rely on the high SNR and high resolution spectra only obtainable by direct imaging spectroscopy, but a deeper understanding of systematics in atmospheric models is necessary to fully exploit these datasets.

Online content

Any methods, additional references, Nature Portfolio reporting summaries, source data, extended data, supplementary information, acknowledgements, peer review information; details of author contributions and competing interests; and statements of data and code availability are available at https://doi.org/10.1038/s41586-025-09174-w.

1. Currie, T. et al. Direct imaging and spectroscopy of extrasolar planets. In Proc. *Protostars and Planets VII* (eds Inutsuka, S. et al.) Vol. 534, 799 (Astronomical Society of the Pacific, 2023).
2. Dyrek, A. et al. SO$_2$, silicate clouds, but no CH$_4$ detected in a warm Neptune. *Nature* **625**, 51–54 (2024).
3. Welbanks, L. et al. A high internal heat flux and large core in a warm Neptune exoplanet. *Nature* **630**, 836–840 (2024).
4. Grant, D. et al. JWST-TST DREAMS: quartz clouds in the atmosphere of WASP-17b. *Astrophys. J. Lett.* **956**, L32 (2023).
5. Tsai, S.-M. et al. Photochemically produced SO$_2$ in the atmosphere of WASP-39b. *Nature* **617**, 483–487 (2023).
6. Sing, D. K. et al. A continuum from clear to cloudy hot-Jupiter exoplanets without primordial water depletion. *Nature* **529**, 59–62 (2016).
7. Bell, T. J. et al. Nightside clouds and disequilibrium chemistry on the hot Jupiter WASP-43b. *Nat. Astron.* **8**, 879–898 (2024).
8. Suárez, G. et al. Ultracool dwarfs observed with the Spitzer infrared spectrograph: equatorial latitudes in L dwarf atmospheres are cloudier. *Astrophys. J. Lett.* **954**, L6 (2023).
9. Miles, B. E. et al. The JWST Early-release Science Program for Direct Observations of Exoplanetary Systems II: a 1 to 20 μm spectrum of the planetary-mass companion VHS 1256-1257 b. *Astrophys. J. Lett.* **946**, L6 (2023).
10. Sun, Q. et al. A revisit of the mass-metallicity trends in transiting exoplanets. *Astron. J.* **167**, 167 (2024).
11. Bohn, A. J. et al. Two directly imaged, wide-orbit giant planets around the young, solar analog TYC 8998-760-1. *Astrophys. J. Lett.* **898**, L16 (2020).
12. Nielsen, E. L. et al. The Gemini Planet Imager Exoplanet Survey: giant planet and brown dwarf demographics from 10 to 100 au. *Astron. J.* **158**, 13 (2019).
13. Vigan, A. et al. The SPHERE infrared survey for exoplanets (SHINE). III. The demographics of young giant exoplanets below 300 au with SPHERE. *Astron. Astrophys.* **651**, A72 (2021).
14. Zhang, Y. et al. The ^{13}CO-rich atmosphere of a young accreting super-Jupiter. *Nature* **595**, 370–372 (2021).
15. Zhang, Y. et al. The ESO SupJup Survey. III. Confirmation of ^{13}CO in YSES 1 b and atmospheric detection of YSES 1 c with CRIRES+. *Astron. J.* **168**, 246 (2024).
16. Cushing, M. C. et al. A *Spitzer* infrared spectrograph spectral sequence of M, L, and T dwarfs. *Astrophys. J.* **648**, 614–628 (2006).
17. Cushing, M. C. et al. Atmospheric parameters of field L and T dwarfs. *Astrophys. J.* **678**, 1372–1395 (2008).
18. Marley, M. S., Saumon, D. & Goldblatt, C. A patchy cloud model for the L to T dwarf transition. *Astrophys. J. Lett.* **723**, L117 (2010).
19. Suárez, G. & Metchev, S. Ultracool dwarfs observed with the Spitzer infrared spectrograph - II. Emergence and sedimentation of silicate clouds in L dwarfs, and analysis of the full M5-T9 field dwarf spectroscopic sample. *Mon. Not. R. Astron. Soc.* **513**, 5701–5726 (2022).
20. Petrus, S. et al. A new take on the low-mass brown dwarf companions on wide orbits in Upper-Scorpius. *Astron. Astrophys.* **633**, A124 (2020).
21. Petrus, S. et al. X-SHYNE: X-shooter spectra of young exoplanet analogs. I. A medium-resolution 0.65–2.5 μm one-shot spectrum of VHS 1256–1257 b. *Astron. Astrophys.* **670**, L9 (2023).
22. Calamari, E. et al. Predicting cloud conditions in substellar mass objects using ultracool dwarf companions. *Astrophys. J.* **963**, 67 (2024).
23. Mollière, P. et al. petitRADTRANS: a Python radiative transfer package for exoplanet characterization and retrieval. *Astron. Astrophys.* **627**, A67 (2019).
24. Petrus, S. et al. The JWST Early Release Science Program for Direct Observations of Exoplanetary Systems. V. Do self-consistent atmospheric models represent JWST spectra? A showcase with VHS 1256-1257 b. *Astrophys. J. Lett.* **966**, L11 (2024).
25. Charnay, B. et al. A self-consistent cloud model for brown dwarfs and young giant exoplanets: comparison with photometric and spectroscopic observations. *Astrophys. J.* **854**, 172 (2018).
26. Burrows, A. & Sharp, C. Chemical equilibrium abundances in brown dwarf and extrasolar giant planet atmospheres. *Astrophys. J.* **512**, 843–863 (1999).
27. Barman, T. S., Macintosh, B., Konopacky, Q. M. & Marois, C. Clouds and chemistry in the atmosphere of extrasolar planet HR8799b. *Astrophys. J.* **733**, 65 (2011).
28. Tremblin, P. et al. Cloudless atmospheres for young low-gravity substellar objects. *Astrophys. J.* **850**, 46 (2017).
29. Bowler, B. P. et al. Rotation periods, inclinations, and obliquities of cool stars hosting directly imaged substellar companions: spin-orbit misalignments are common. *Astron. J.* **165**, 164 (2023).
30. Stassun, K. G. et al. The revised *TESS* input catalog and candidate target list. *Astron. J.* **158**, 138 (2019).
31. Marley, M., Ackerman, A., Cuzzi, J. & Kitzmann, D. in *Comparative Climatology of Terrestrial Planets*(eds Mackwell, S.J. et al.) 367–391 (Univ. Arizona Press, 2013).
32. Luna, J. L. & Morley, C. V. Empirically determining substellar cloud compositions in the era of the James Webb Space Telescope. *Astrophys. J.* **920**, 146 (2021).
33. Cushing, M. C., Rayner, J. T., Davis, S. P. & Vacca, W. D. FeH absorption in the near-infrared spectra of late M and L dwarfs. *Astrophys. J.* **582**, 1066–1072 (2003).
34. Moran, S. E., Marley, M. S. & Crossley, S. D. Neglected silicon dioxide polymorphs as clouds in substellar atmospheres. *Astrophys. J. Lett.* **973**, L3 (2024).
35. van Holstein, R. et al. A survey of the linear polarization of directly imaged exoplanets and brown dwarf companions with SPHERE-IRDIS. First polarimetric detections revealing disks around DH Tau B and GSC 6214-210 B. *Astron. Astrophys.* **647**, A21 (2021).
36. Benisty, M. et al. A circumplanetary disk around PDS70c. *Astrophys. J. Lett.* **916**, L2 (2021).
37. Cugno, G. et al. Mid-infrared spectrum of the disk around the forming companion GQ Lup B revealed by JWST/MIRI. *Astrophys. J. Lett.* **966**, L21 (2024).
38. Perrin, M. D. et al. Updated point spread function simulations for JWST with WebbPSF. In Proc. *Space Telescopes and Instrumentation 2014: Optical, Infrared, and Millimeter Wave*, 91433X (SPIE, 2014).
39. Horne, K. An optimal extraction algorithm for CCD spectroscopy. *Publ. Astron. Soc. Pac.* **98**, 609–617 (1986).
40. Nasedkin, E. et al. Four-of-a-kind? Comprehensive atmospheric characterisation of the HR 8799 planets with VLTI/GRAVITY. *Astron. Astrophys.* **687**, A298 (2024).
41. Buchner, J. et al. X-ray spectral modelling of the AGN obscuring region in the CDFS: Bayesian model selection and catalogue. *Astron. Astrophys.* **564**, A125 (2014).
42. Bailer-Jones, C., Rybizki, J., Fouesneau, M., Mantelet, G. & Andrae, R. Estimating distance from parallaxes. IV. Distances to 1.33 billion stars in *Gaia* data release 2. *Astron. J.* **156**, 58 (2018).
43. Nasedkin, E., Mollière, P. & Blain, D. Atmospheric retrievals with petitRADTRANS. *J. Open Source Softw.* **9**, 5875 (2024).
44. Feroz, F., Hobson, M. & Bridges, M. MULTINEST: an efficient and robust Bayesian inference tool for cosmology and particle physics. *Mon. Not. R. Astron. Soc.* **398**, 1601–1614 (2009).

Methods

Observations, data reduction and PSF model subtraction

The data presented are from the Cycle 1 observing program 2044 (principal investigator K.K.W.H.), with details of instrument settings and exposure times given in Extended Data Table 1. Observations were obtained using the NIRSpec IFU prism mode. We placed the IFU field of view to include both planets with the bright host star outside. However, two of the four dither positions placed YSES-1 c on the edge of the field of view. For MIRI, the low-resolution spectroscopy mode observed the two planets sequentially using a two-point nod.

We performed initial reduction steps using the JWST data pipeline v.1.13.4 and CRDS context 1125. For the NIRSpec data, we performed pixel outlier detection using all four dithered exposures, then produced the final spectral datacube using only the two dithers for which YSES-1 c was within the field of view (Extended Data Fig. 1). To remove the host star point spread function (PSF), we conducted PSF subtraction using models generated with WebbPSF[38]. We fit the 3.0 μm slice of the datacube and iterated to optimize by least squares the alignment between the model and the host star location. We then iterated over all wavelengths to generate model PSFs and subtract them from the science data. Each wavelength was fit with a multiplicative scale factor to minimize the residuals over a region around each planet to produce a PSF-subtracted datacube (Extended Data Fig. 1).

For the MIRI LRS data, the PSF subtraction relied on removing a scaled numerical model of the PSF. We developed a custom code to forward model MIRI LRS data, available on GitHub (https://github.com/mperrin/miri_lrs_fm). We fit a forward model of the planet as a point source within the slit, the wings of the offset host star outside of the slit and the diffuse thermal sky background. We iterated to optimize position offsets and flux scale factors. We generated a series of monochromatic PSFs, shifted at each wavelength according to the spectral dispersion profile and summed to generate a synthetic two-dimensional (2D) spectrum. We scaled the flux by a model of the spectral energy distribution of the host star and subtracted the model from the science data, and fit an overall flux scale factor and background offset varying with wavelength. The two nods were subtracted from each other to remove the observatory thermal background. The PSF subtraction resulted in a notable decrease in systematics between the two nods (See Extended Data Figs. 2–3).

Spectral extraction

We extracted the spectra from the PSF-subtracted NIRSpec datacube by PSF-fitting photometry using a 2D Gaussian PSF model plus a constant background term. We fit the position of each planet after summing over the wavelength axis. Next, we iterated over wavelength and fitted a 2D Gaussian + constant at each wavelength while holding the position fixed. Bad pixels were masked and not included. We summed the 2D Gaussian model flux at each wavelength to obtain companion spectra. We drew 1,000 values from the Gaussian model parameter posterior, its uncertainties from the least squares fit. We evaluated the companion flux for each of these 1,000 draws and reported lower and upper flux uncertainties based on the 16th and 84th percentiles and propagated the JWST data reduction pipeline uncertainties.

For the MIRI data, we extracted spectra using PSF-profile-weighted extraction[39]. We again generated a dispersed PSF model of the companion in each nod, and the model PSF cross-dispersion spatial profile at each wavelength was used to compute a weighted sum of the 2D spectral image. The resulting spectra for each nod were then averaged and uncertainties propagated. This was repeated for both planets. Note that the sensitivity of MIRI LRS decreases sharply beyond 12 μm resulting in lower SNR at longer wavelengths.

Atmospheric forward modelling

We forward model the atmospheric spectra using the self-consistent cloudy atmospheric model grid Exo-REM[22]. Exo-REM assumes radiative–convective equilibrium, non-equilibrium chemistry for a limited number of molecules (CO, CH_4, CO_2 and NH_3) and the formation of clouds (iron, Na_2S, KCl, silicates and water). Exo-REM covers $T_{\rm eff}$ = 400–2,000 K and includes molecular absorptions with the rovibrational bands of H_2O, CH_4, CO, CO_2, NH_3, PH_3, TiO, VO and FeH. The grid also includes atomic absorptions with resonant lines from Na and K, and collision-induced absorptions of H_2–H_2 and H_2–He. The particle size distributions are log-normal with a constant effective variance of 0.3. We explore ranges of surface gravities ($\log(g)$ = 3.0–5.0 dex), metallicities ([M/H] = −0.5 to 0.5) and C/O ratios (0.1–0.8).

We used the ForMoSA code[23,24] with a nested sampling algorithm (pyMultinest[41]) and optimized grid interpolations. The resolution and spectral coverage of the grid are adapted to the data through a Gaussian convolution followed by binning. The luminosity dilution factor $C_k = (R/d)^2$ is calculated for the synthetic spectra considering $d = 94.6 \pm 0.3$ pc (ref. 42). We combine the atmospheric model with a CPD model for YSES-1 b consisting of a blackbody defined by a temperature $T_{\rm CPD}$ and a radius $R_{\rm CPD}$). All priors used are in Extended Data Table 2.

The entire spectral range was used for YSES-1 b and wavelengths less than 7.5 μm were used for YSES-1 c. However, at medium resolution, self-consistent models struggled to reproduce the data over a wide spectral range inducing under-estimated errors. These errors reflect the good SNR of the data propagated through the Bayesian inversion, but the errors are dominated by systematic errors in the self-consistent models. To mitigate this, we progressively increased the uncertainties until the reduced χ^2 of the previous fit reached 1. If the reduced χ^2 fell within the range of 0.5–1.5, we adopted the corresponding error values for the data and the posterior distributions.

Atmospheric retrievals

We used pRT v.3.2.0a16 to perform atmospheric retrievals on the planet spectra[26,43]. pRT relies on the pyMultinest[41,44,45] implementation of nested sampling[46] to sample the parameter space, estimate the posterior probability distributions and calculate the model evidence. We used 1,000 live points with a sampling efficiency of 0.3 for model comparison of 10^7–10^8 models. All priors used are in Extended Data Table 2. We used the entire wavelength range for YSES-1 b and removed a low SNR region from 0.6 μm to 0.88 μm for YSES-1 c.

Our model consists of a temperature profile, a chemical model and a cloud parameterization, at 134 discrete pressure levels spaced between 1,000 bar and 10^{-6} bar, with a higher resolution grid at the location of cloud condensation[40,47]. The temperature profile used is taken from ref. 48, in which the free parameters of the model are the temperature gradient at 10 equidistant points in pressure space[48]. Our parameterization extended the retrieved gradients to the top of the atmosphere, rather than isothermal at pressures lower than 10^{-3} bar.

We used a free chemistry approach in which the molecular mass-fraction abundances are free parameters constant with altitude. The remaining atmosphere is a mixture of 76% H_2 and 23% He. For YSES-1 c, we included H_2O (ref. 49), CO (ref. 50), CH_4 (ref. 51), CO_2 (ref. 52), NH_3 (ref. 53), HCN (ref. 54), H_2S (ref. 55), PH_3 (ref. 56), FeH (ref. 57), Na (ref. 58) and K (ref. 59). TiO (ref. 60) and VO (ref. 61) are included for the higher-temperature YSES-1 b. We include collisionally induced absorption from H_2–H_2 and H_2–He, and Rayleigh scattering from H_2 and He. The chemical abundances measured resulted in metallicity relative to solar[62,63] using

$$[M/H] = \log_{10}\frac{\sum_i N_i}{\sum_i N_{i,\odot}},$$

for number fractions N_i and summing over all elements present in the molecular species. The C/O ratio was calculated using the total number of retrieved carbon and oxygen atoms. We exclude the alkali metals, as the retrieved Na abundance is unphysically large because of the steep NIR slope possibly affected by cloud absorption.

We retrieve the mean cloud particle size, the width of log-normal distribution of particle sizes and the mass fraction at the cloud base decreasing as a power law with a slope of f_{SED}. We included both an iron cloud and a silicate cloud. We compared Mie-scattering, crystalline $MgSiO_3$ (ref. 64) and $Mg_{0.5}Fe_{0.5}SiO_3$ (ref. 64) compositions to determine the best-fit mid-infrared absorption feature. An amorphous $MgSiO_3$ composition was also tested, performing worse than the crystalline particles. We retrieve a patchiness parameter for the silicate cloud, whereas the deeper iron cloud is assumed to completely envelope the planet[65].

Finally, we retrieve parameters of mass and radius to calculate the surface gravity and compute the luminosity dilution factor with $d = 94.6 \pm 0.3$ pc (ref. 42). For YSES-1 b, we include the same circumplanetary disk model from the forward model fits.

The emission spectrum is calculated using correlated-*k* opacities binned to a spectral resolution of 400, then convolved to instrumental spectral resolving power. The resolving power is defined for each wavelength channel and subsequently binned to the instrumental wavelength grid[66]. We present only the most favoured models in this work.

Without error inflation, we measure a lower mass for YSES-1 c ($1.80 \pm 0.07 M_{\mathrm{J}}$), driven by the low surface gravity (3.41 ± 0.02 dex). In Extended Data Fig. 4, we show the retrieved temperature profile and emission spectrum of YSES-1 c. The effective temperature measured was $1{,}025 \pm 1$ K and the log bolometric luminosity was -4.7376 ± -0.0003 dex relative to solar. We find a modest enrichment of metals ($[\mathrm{M/H}] = 0.52 \pm 0.01$), and a super-solar gas-phase C/O ratio of 0.798 ± 0.003. Roughly 20% of oxygen can be sequestered in silicate clouds[29,30,67]. Accounting for this sink, we find a bulk C/O ratio of 0.64. Furthermore, we find $[\mathrm{C/H}] = 0.66 \pm 0.01$, $[\mathrm{O/H}] = 0.50 \pm 0.01$ and $[\mathrm{S/H}] = 0.81 \pm 0.01$. Carbon and oxygen are moderately enriched compared with the solar value, whereas the sulfur abundance ratio is strongly enriched. We measure abundances for each of H_2O, CO, CH_4, CO_2, H_2S and K, with the mass fraction abundances (Extended Data Fig. 5).

For YSES-1 b, the retrievals were unable to constrain physically plausible values because of the interactions of the planet and the disk. Therefore, we report only the effective temperature (2002^{+13}_{-9}K), the log bolometric luminosity (-3.2612 ± -0.0007 dex) and the disk temperature (515 ± 4 K), and radius ($17.5 \pm 0.2 R_{\mathrm{J}}$) using a blackbody.

The uncertainties on these measurements reflect the precision of the JWST data, and the reduced χ^2 of our best fit for YSES-1 c is 7.18. To account for model uncertainty, we performed retrievals with error inflation, where $\sigma_{\mathrm{total}} = \sqrt{\sigma_{\mathrm{measured}}{}^2 + 10^b}$, where b is a retrieved parameter[68]. For NIRSpec, we find $\mathrm{b}_{\mathrm{NIRSpec}} = -36.823 \pm 0.013$, where the typical order of the measured uncertainties is 1×10^{-19} W m^{-2} μm^{-1}. The inflation term is more dominant for MIRI data, $b_{\mathrm{MIRI}} = -36.765 \pm 0.021$, with the typical scale of the measured MIRI uncertainties of about 2×10^{-20} W m^{-2} μm^{-1}. Error inflation causes lower precision on the measured parameters (χ^2/ν near 1). The bulk metallicity decreases to approximately solar and the planet mass decreases to an unphysically small estimate of $0.588 \pm 0.02 M_{\mathrm{J}}$. This method allows a better goodness of fit, but the parameters retrieved present unphysical results. Models accounting for three-dimensional effects improved line lists, and more detailed cloud parameterizations will be required to fully exploit the JWST data.

Silicate feature cloud modelling

We defined the silicate feature of YSES-1 c as a flux ratio between the best-fit cloudy Exo-REM model, excluding the silicate feature ($T_{\mathrm{eff}} = 950$ K, $\log(g) = 3.5$, $[\mathrm{M/H}] = 0$, $\mathrm{C/O} = 0.60$) and the YSES-1 c spectrum.

The silicate feature fitting was performed using VIRGA[69,70] and PICASO[71,72] to model different types of silicate clouds with varying cloud properties. The thermal and chemical profiles from the Exo-REM model were input into PICASO to produce a cloud-free spectrum between 7 μm and 12 μm. Rather than using the standard EddySed formulation, VIRGA was used to add ad hoc clouds with varying chemical composition, crystalline and amorphous optical properties, particle sizes, cloud base pressures and cloud column number densities. These clouds with updated optical properties were added to the cloud-free Exo-REM thermal and chemical profiles, and PICASO was used to produce new spectra[32]. Silicate features for each cloud model were calculated as a flux ratio between the Exo-REM spectrum with the cloud and the cloud-free Exo-REM spectrum between 7 μm and 12 μm. The silicate feature of YSES-1 c was then compared with all of the silicate features modelled with VIRGA and PICASO.

The cloud species considered were SiO_2 amorphous[73,74], Mg_2SiO_4 (amorphous[75] and crystalline[76]), $MgSiO_3$ (amorphous[77] and crystalline[64]), crystalline $MgSiO_3$ at three temperatures (10 K, 300 K and 928 K) (ref. 78) and several amorphous pyroxene species ($Mg_{0.95}Fe_{0.05}SiO_3$, $Mg_{0.8}Fe_{0.2}SiO_3$, $Mg_{0.5}Fe_{0.5}SiO_3$ and $Mg_{0.4}Fe_{0.6}SiO_3$) (ref. 77). Cloud base pressures ranged from 0.1 bar to 0.0001 bar, and the vertical extent of the cloud was set using an f_{SED} value of 1, which was held constant for all models. Cloud column number densities ranged from 10^7 to 10^9 particles per cm^2. Particle size distributions were tightly focused (a log-normal distribution with $\sigma = 1.2$) around values ranging from 0.01 μm to 10 μm. Particle size distributions were held constant with pressure. Cloud combination models used a mixture of amorphous $MgSiO_3$ and Mg_2SiO_4 with the same cloud base pressures and mean particle sizes but differing fractions of the total column number density. The combination models fit the observed feature using a mean particle size of 0.1 μm, a cloud base pressure of 1 (−0.2, +0.6) millibar, and a column density of $1 (\pm 0.1) \times 10^8$ cm^{-2}. The precise combination of amorphous $MgSiO_3$ and Mg_2SiO_4 varied between 60% and 90% $MgSiO_3$ based on the other parameters. The mass density of cloud particles at the base of the cloud for the best-fit cloud models quoted above were between 2.1×10^{-7} g cm^{-3} and 3.7×10^{-7} g cm^{-3}. We note that mass density at the base of the cloud can also be achieved with smaller particle sizes and larger column densities, so the mean particle size of 0.1 μm is only an upper limit. Additional models with the particle size distribution determined by a Hansen distribution did not change the colour of the feature or the inferred composition. Extended Data Fig. 6 shows the impact of changing each of these parameters on the resulting silicate feature. Clouds with mean particle radius of 1 μm and 10 μm blocked almost all flux in these wavelengths and resulted in flux ratios an order of magnitude larger than the 0.1 μm and 0.01 μm models and, therefore, are not included in Extended Data Fig. 6. We note that the low-resolution spectrometer spectrum SNR drops closer to 12 μm because of the faintness of YSES-1 c (Extended Data Fig. 2). We, therefore, considered only the first half of the feature. Only deep MIRI MRS observations can obtain the SNR needed to characterize the entire silicate cloud feature beyond 12 μm.

Empirical fitting of the infrared excess for YSES-1 b

We fit the infrared excess using a size distribution of silicate grains from sub-μm- to mm-sized grains. We subtracted an Exo-REM model containing only the atmosphere emission to isolate the infrared excess. We omitted data at wavelengths greater than 7 μm as the water vapour in the atmosphere creates absorption at 6.3 μm. There is a clear 10 μm emission feature consistent with μm-sized silicate grains, explaining why simple blackbody emission did not fit the excess[79]. Blackbody grains are large (>10 μm), and their thermal emission produces a broad feature. Solid-state emission features are more narrow and indicate the presence of smaller sub-μm- to μm-sized dust. We constrain the grain size distribution of the dust by fitting the emission excess assuming that the grains are spherical (Mie theory) and composed of amorphous olivine ($MgFeSiO_4$; ref. 77) as it is the most common silicate species detected in the interstellar medium and protoplanetary disks[80]. Although crystalline silicates are observed in T Tauri disks, these silicates have distinctive sharp spectral features not observed in our spectrum[81–83].

We model the thermal emission assuming that the dust is composed of both small silicate grains and large blackbody grains. The particle size distribution for the small grains is a power law consistent with collisional equilibrium using

$$F_\nu = C_1 \int_{a_{\min}}^{a_{\max}} \pi a^2 a^{-3.5} Q_{\rm abs}(a) B_\nu(T_{\rm sil}) da + C_2 B_\nu(T_{\rm bb}),$$

where a is the grain size, $a_{\min}$ is the minimum grain size, $a_{\max}$ is the maximum grain size, $Q_{\rm abs}$ is the absorption efficiency, $T_{\rm sil}$ is the temperature of the small silicate grains and $T_{\rm bb}$ is the temperature of the large blackbody grains[83]. In our fit, we fix $a_{\max}$ to 1 mm and use an Markov Chain Monte Carlo to estimate the best-fitting values for $a_{\min}$, $T_{\rm sil}$, $T_{\rm bb}$, C_1 and C_2. We estimate $a_{\min} = 0.71\ \mu$m, $T_{\rm sil} = 488$ K, $T_{\rm bb} = 602$ K, $C_1 = 801$ and $C_2 = 7{,}080$.

From the temperature of the silicates, we calculated the distances of grains from the planet by assuming that the grains are in thermal equilibrium and heated by YSES-1 b. The distance of the μm-sized grains in the limit that $2\pi a \ll \lambda$, is

$$d = \frac{1}{2}\left(\frac{T_{\rm YSES\text{-}1\,b}}{T_{\rm sil}}\right)^{\frac{5}{2}} R_{\rm YSES\text{-}1\,b},$$

where $T_{\rm YSES\text{-}1b}$ is the temperature of YSES-1 b and $R_{\rm YSES\text{-}1b}$ is its radius. For the blackbody-emitting grains,

$$d = \frac{1}{2}\left(\frac{T_{\rm YSES\text{-}1\,b}}{T_{\rm sil}}\right)^{2} R_{\rm YSES\text{-}1\,b}.$$

The distances of the silicates are $10.5 \pm 1.7 R_{\rm J}$, and the blackbody grains are $17.6 \pm 3.7 R_{\rm J}$.

The mass of the circumplanetary disk is dominated by the material in large, m- to km-sized objects, but they do not contribute to the 10-μm emission. This feature is caused by small particles less than 10 μm. Thus, the dust mass calculated for the CPD is from small dust particles, which is a small fraction of the true mass.

To calculate the mass of the circumplanetary disk, the size distribution was integrated:

$$M_{\rm dust} = C_1 {d^2}_{\rm YSES\text{-}1} \int_{a_{\min}}^{a_{\max}} \left(\frac{4\pi}{3} a^3\right) a^{-3.5} \rho da.$$

where C_1 is the constant of proportionality fit for the μm-sized silicate emission, $d_{\rm YSES\text{-}1}$ is the distance to YSES-1 b from the observer, a is the particle size, $a_{\min}$ and $a_{\max}$ are the minimum and maximum grain sizes fit to silicate emission, respectively, and $\rho = 3.72$ g cm^{-3} is the mass density of olivine. The resulting dust mass is about $6.472 \pm 0.4 \times 10^{15}$ g, which is 8.8×10^{-8} times the mass of the moon of Earth.

Data availability

The data used in this paper are associated with the JWST program GO 2044 and are available from the Mikulski Archive for Space Telescopes (https://mast.stsci.edu). The dataset is available at https://doi.org/10.17909/a2vk-mh23. The data used for host star measurements are associated with the UVES/VLT Program (106.20ZM.00) and the XShooter/VLT Program (103.2008.001) and are available from the ESO Archive (https://archive.eso.org/).

Code availability

This study made use of the following software codes to analyse the data: NumPy[84], astropy[85], matplotlib[86], SciPy[87], pandas[88], ForMoSA[20,21], VIRGA[69,70], PICASO[71,72], pyMultinest[41], WebbPSF[38] and petitRADTRANS[23]. The spectral extraction script used for the MIRI LRS data is available at GitHub (https://github.com/mperrin/miri_lrs_fm).

45. Feroz, F., Hobson, M. P., Cameron, E. & Pettitt, A. N. Importance nested sampling and the MultiNest algorithm. *Open J. Astrophys.* **2**, 10 (2019).
46. Skilling, J. Nested sampling. *AIP Conf. Proc.* **735**, 395–405 (2004).
47. Mollière, P. et al. Retrieving scattering clouds and disequilibrium chemistry in the atmosphere of HR 8799e. *Astron. Astrophys.* **640**, A131 (2020).
48. Zhang, Z. et al. ELemental abundances of Planets and brown dwarfs Imaged around Stars (ELPIS). I. Potential metal enrichment of the exoplanet AF Lep b and a novel retrieval approach for cloudy self-luminous atmospheres. *Astron. J.* **166**, 198 (2023).
49. Polyansky, O. L. et al. ExoMol molecular line lists XXX: a complete high-accuracy line list for water. *Mon. Not. R. Astron. Soc.* **480**, 2597–2608 (2018).
50. Rothman, L. S. et al. HITEMP, the high-temperature molecular spectroscopic database. *J. Quant. Spectrosc. Radiat. Transf.* **111**, 2139–2150 (2010).
51. Guest, E. R., Tennyson, J. & Yurchenko, S. N. Predicting the rotational dependence of line broadening using machine learning. *J. Mol. Spectrosc.* **401**, 111901 (2024).
52. Yurchenko, S. N., Mellor, T. M., Freedman, R. S. & Tennyson, J. ExoMol line lists – XXXIX. Ro-vibrational molecular line list for CO_2. *Mon. Not. R. Astron. Soc.* **496**, 5282–5291 (2020).
53. Coles, P. A., Yurchenko, A.-S. N. & Tennyson, J. ExoMol molecular line lists XXXV: a rotation-vibration line list for hot ammonia. *Mon. Not. R. Astron. Soc.* **490**, 4638–4647 (2019).
54. Barber, R. J. et al. ExoMol line lists - III. An improved hot rotation-vibration line list for HCN and HNC. *Mon. Not. R. Astron. Soc.* **437**, 1828–1835 (2014).
55. Azzam, A. A., Yurchenko, S. N., Tennyson, J. & Naumenko, O. V. ExoMol line lists XVI: a hot line list for H_2S. *Mon. Not. R. Astron. Soc.* **460**, 4063–4074 (2016).
56. Sousa-Silva, C., Al-Refaie, A. F., Tennyson, J. & Yurchenko, S. N. ExoMol line lists - VII. The rotation-vibration spectrum of phosphine up to 1500K. *Mon. Not. R. Astron. Soc.* **446**, 2337–2347 (2015).
57. Wende, S., Reiners, A., Seifahrt, A. & Bernath, P. CRIRES spectroscopy and empirical line-by-line identification of FeH molecular absorption in an M dwarf. *Astron. Astrophys.* **523**, A58 (2010).
58. Allard, N. F., Spiegelman, F., Leininger, T. & Mollière, P. New study of the line profiles of sodium perturbed by H_2. *Astron. Astrophys.* **628**, A120 (2019).
59. Allard, N. F., Spiegelman, F. & Kielkopf, J. F. K-H_2 line shapes for the spectra of cool brown dwarfs. *Astron. Astrophys.* **589**, A21 (2016).
60. McKemmish, L. K. et al. ExoMol molecular line lists - XXXIII. The spectrum of titanium oxide. *Mon. Not. R. Astron. Soc.* **488**, 2836–2854 (2019).
61. McKemmish, L. K., Yurchenko, S. N. & Tennyson, J. ExoMol line lists - XVIII. The high-temperature spectrum of VO. *Mon. Not. R. Astron. Soc.* **463**, 771–793 (2016).
62. Asplund, M., Grevesse, N., Sauval, A. J. & Scott, P. The chemical composition of the sun. *Annu. Rev. Astron. Astrophys.* **47**, 481–522 (2009).
63. Ackerman, A. S. & Marley, M. S. Precipitating condensation clouds in substellar atmospheres. *Astrophys. J.* **556**, 872–884 (2001).
64. Jäger, C. et al. Steps toward interstellar silicate mineralogy. IV. The crystalline revolution. *Astron. Astrophys.* **339**, 904–916 (1998).
65. Vos, J. M. et al. Patchy forsterite clouds in the atmospheres of two highly variable exoplanet analogs. *Astrophys. J.* **944**, 138 (2023).
66. Greenfield, P. & Miller, T. The Calibration Reference Data System. *Astron. Comput.* **16**, 41–53 (2016).
67. Fonte, S. et al. Oxygen depletion in giant planets with different formation histories. *Mon. Not. R. Astron. Soc.* **520**, 4683–4695 (2023).
68. Line, M. R. et al. Uniform atmospheric retrieval analysis of ultracool dwarfs. I. Characterizing benchmarks, Gl 570D and HD 3651B. *Astrophys. J.* **807**, 183 (2015).
69. Batalha, N., Rooney, C. & Mukherjee, S. natashabatalha/virga: Initial release (v0.0). *Zenodo* https://doi.org/10.5281/zenodo.3759888 (2020).
70. Rooney, C. M., Batalha, N. E., Gao, P., Marley, M. S. & New, A. A new sedimentation model for greater cloud diversity in giant exoplanets and brown dwarfs. *Astrophys. J.* **925**, 33 (2022).
71. Batalha, N., Rooney, C. natashabatalha/picaso: Release 2.1. *Zenodo* https://doi.org/10.5281/zenodo.4206648 (2020).
72. Batalha, N. E., Marley, M. S., Lewis, N. K. & Fortney, J. J. Exoplanet Reflected-light Spectroscopy with PICASO. *Astrophys. J.* **878**, 70 (2019).
73. Palik, E. D. (ed.) *Handbook of Optical Constants of Solids* (Academic Press, 1985).
74. Wetzel, S. et al. Laboratory measurement of optical constants of solid SiO and application to circumstellar dust. *Astron. Astrophys.* **553**, A92 (2013).
75. Jäger, C., Dorschner, J., Mutschke, H., Posch, T. & Henning, T. Steps toward interstellar silicate mineralogy. VII. Spectral properties and crystallization behaviour of magnesium silicates produced by the sol-gel method. *Astron. Astrophys.* **408**, 193–204 (2003).
76. Mutschke, H. & Mohr, P. Far-infrared continuum absorption of forsterite and enstatite at low temperatures. *Astron. Astrophys.* **625**, A61 (2019).
77. Dorschner, J. et al. Steps toward interstellar silicate mineralogy. II. Study of Mg-Fe-silicate glasses of variable composition. *Astron. Astrophys.* **300**, 503 (1995).
78. Zeidler, S., Mutschke, H. & Posch, T. Temperature-dependent Infrared Optical Constants of Olivine and Enstatite. *Astrophys. J.* **798**, 125 (2015).
79. Li, A. & Greenberg, J. M. The dust extinction, polarization and emission in the high-latitude cloud toward HD 210121. *Astron. Astrophys.* **339**, 591–600 (1998).
80. Henning, T. Cosmic silicates. *Annu. Rev. Astron. Astrophys.* **48**, 21–46 (2010).
81. Kessler-Silacci, J. et al. *c2d Spitzer* IRS spectra of disks around T Tauri stars. I. Silicate emission and grain growth. *Astrophys. J.* **639**, 275–291 (2006).
82. Bouwman, J. et al. The formation and evolution of planetary systems: grain growth and chemical processing of dust in T Tauri systems. *Astrophys. J.* **683**, 479–498 (2008).
83. Chen, C. et al. Erratum: "Spitzer IRS Spectroscopy of IRAS-Discovered Debris Disks" (ApJS, 166, 351, [2006]). *Astrophys. J.* **177**, 417 (2008).
84. Harris, C. et al. Array programming with NumPy. *Nature* **585**, 4357–4362 (2020).

85. Astropy Collaboration. et al. The Astropy Project: sustaining and growing a community-oriented open-source project and the latest major release (v5.0) of the core package. *Astrophys. J.* **935**, 167 (2022).
86. Hunter, J. D. Matplotlib: a 2D graphics environment. *Comput. Sci. Eng.* **9**, 90–95 (2007).
87. Virtanen, P. et al. SciPy 1.0: fundamental algorithms for scientific computing in Python. *Nat. Methods* **17**, 261–272 (2020).
88. McKinney, W. Data structures for statistical computing in Python. In *Proc. Python in Science Conference* 56–61 (SciPy, 2010).

Acknowledgements S.P. is supported by the ANID FONDECYT postdoctoral program no. 3240145 and an appointment to the NASA Postdoctoral Program at the NASA–Goddard Space Flight Center, administered by Oak Ridge Associated Universities under contract with NASA. V.D. acknowledges the financial contribution from PRIN MUR 2022 (code 2022YP5ACE) funded by the European Union—NextGeneration EU. This work is based on observations made with the NASA/ESA/CSA JWST. The data were obtained from the Mikulski Archive for Space Telescopes at the Space Telescope Science Institute, which is operated by the Association of Universities for Research in Astronomy, under NASA contract NAS 5-03127 for JWST. These observations are associated with program JWST-GO-02044. Support for program JWST-GO-02044 was provided by NASA through a grant from the Space Telescope Science Institute.

Author contributions All authors contributed to the paper, with some specific contributions as follows. K.K.W.H., M.P., Q.M.K., C.A.T., J.-B.R., C.V.M., E.G., K.W.-D., E.R., L.P., M.B., V.D., S.P., T.B., J.G., R.J.D.R., B.R. and G.C. aided in the development of the original proposal and made notable contributions to the overall design of the program. M.P. and K.K.W.H. generated the observing plan with input from the team. M.P. conducted the data reduction and starlight subtraction and performed the MIRI spectral extraction, and J.K. and K.K.W.H. co-led the spectral extraction of NIRSpec prism. M.R. led the cloud modelling effort, S.P. led the forward modelling effort and silicate index empirical analysis, E.N. led the retrieval effort, and C.I. led the thermal modelling with guidance from C.C.; P.P.-B. implemented the ability to fit a CPD in our forward modelling framework. M.K., Y.Z., S.E.M., W.O.B., B.R., R.J.D.R. and B.M. aided in the interpretation and made contributions to the writing of this paper. K.K.W.H., M.P., M.R., S.P., E.N. and C.I. generated figures for this paper.

Competing interests The authors declare no competing interests.

Additional information

Supplementary information The online version contains supplementary material available at https://doi.org/10.1038/s41586-025-09174-w.

Correspondence and requests for materials should be addressed to K. K. W. Hoch.

Peer review information *Nature* thanks Hannah Wakeford and the other, anonymous, reviewer(s) for their contribution to the peer review of this work.

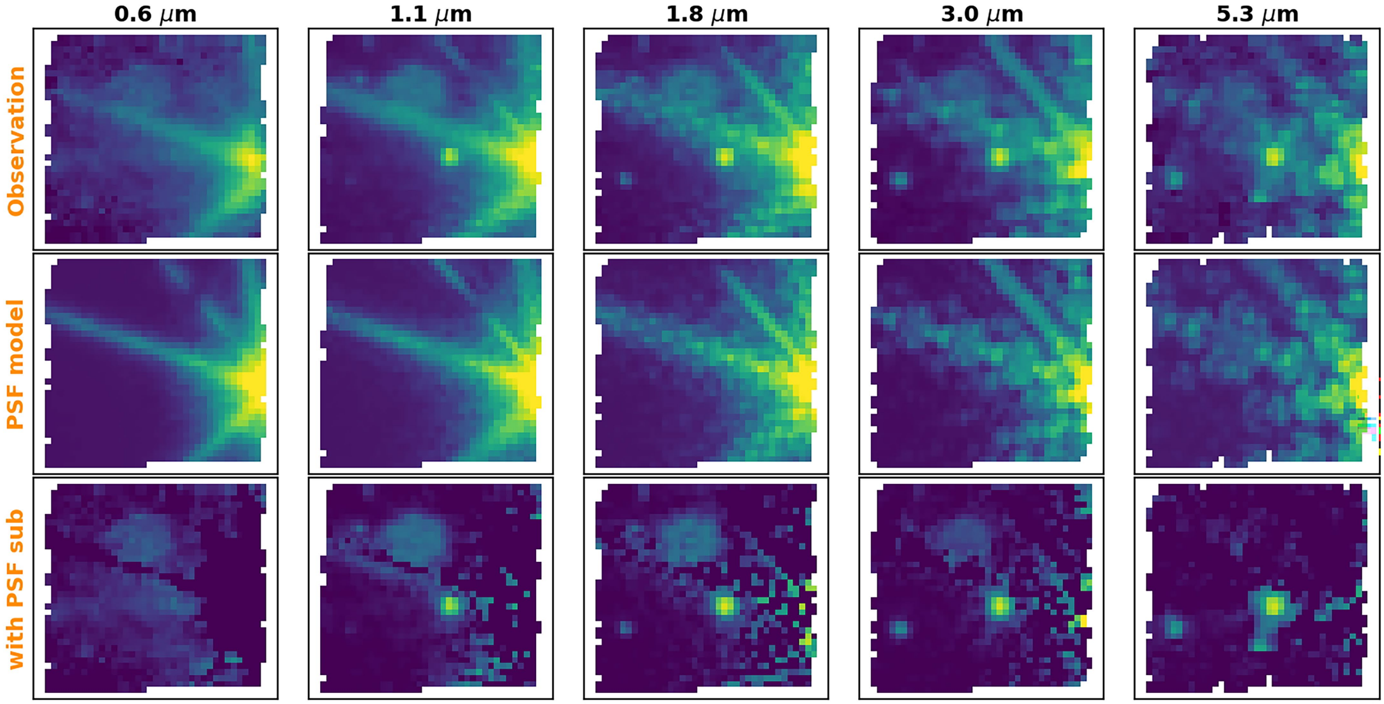

Extended Data Fig. 1 | PSF subtraction of NIRSpec IFU Prism data to remove host star light. The top row shows slices of the combined NIRSpec Prism data cube at five different wavelengths. The data orientation shown here is rotated 90° relative to Fig 1. The middle row shows slices of the PSF model of the host star. The bottom row shows slices of the resultant PSF-subtracted data cube, showing clearer detections of the companions without contamination from the host star. The diffuse roughly circular illumination seen in the third row at wavelengths <= 3 microns is believed to be an optical ghost from reflection within NIRSpec; this is not subtracted by the PSF modelling but owing to its location it has no impact on the extracted spectra of the two planets.

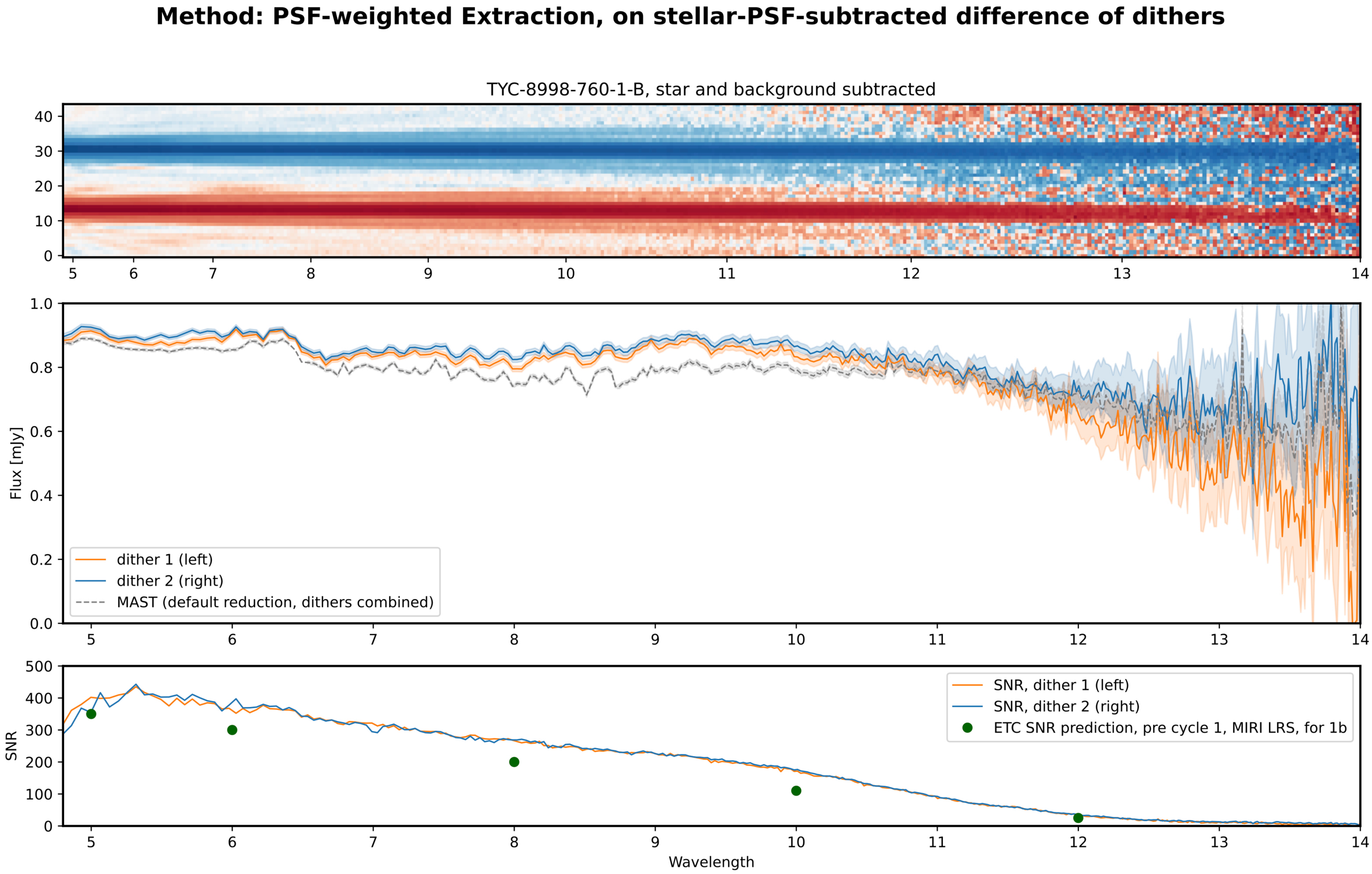

Extended Data Fig. 2 | PSF subtraction and spectral extraction of MIRI LRS data of YSES-1 b. The top panel shows the two separate nods in blue and red for YSES-1 b illustrating the spectral traces after PSF and background subtraction. The middle panel shows spectral extractions from both traces with 3 sigma errors plotted. The black spectra is the average of the two nods. The dashed spectrum shows the MAST reduced and extracted spectra to demonstrate the systematics removed by our PSF subtraction. The bottom panel shows the SNR over wavelength of the respective extracted spectra from the middle panel, as well as the ETC calculations from the Cycle 1 proposal.

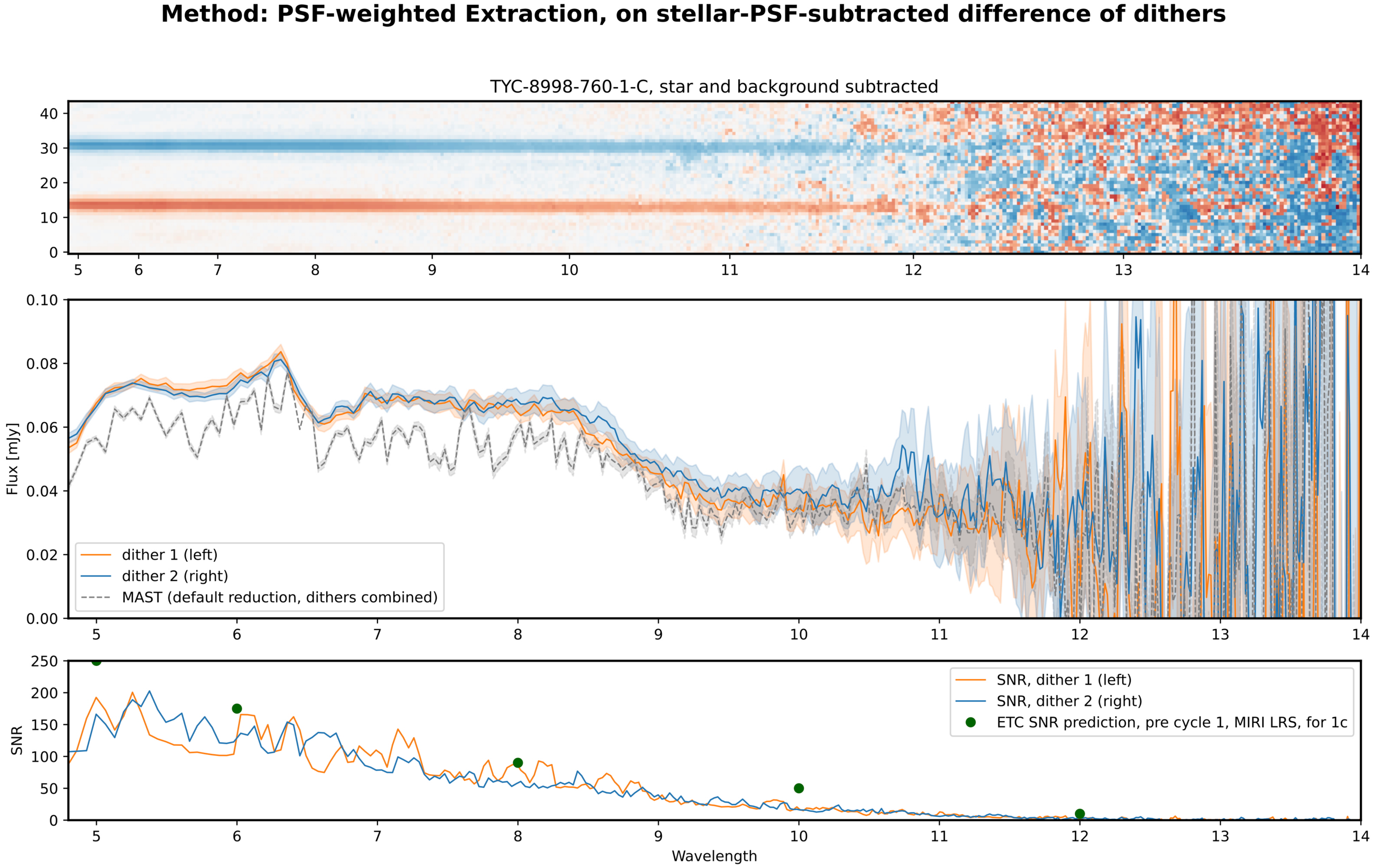

Extended Data Fig. 3 | PSF subtraction and spectral extraction of MIRI LRS data of YSES-1 c. See Extended Data Fig. 2 caption for description.

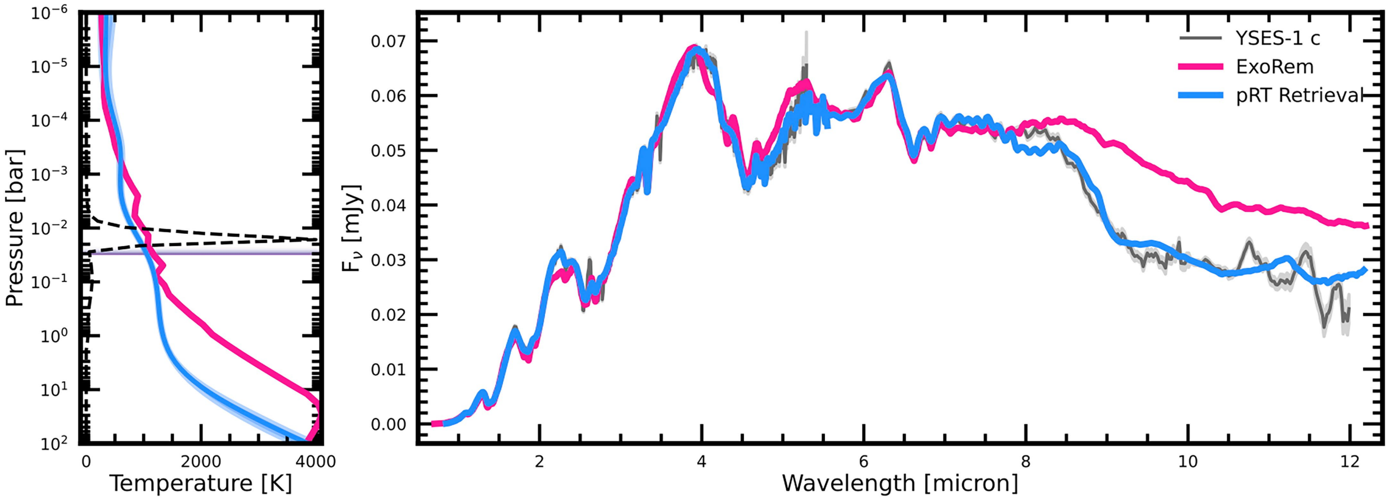

Extended Data Fig. 4 | Forward model and retrieved spectrum compared to YSES-1 c spectrum. Left panel: the pressure-temperature profile for the nearest ExoRem grid point to the best-fit parameters, and a 90% confidence region for the pressure-temperature profile as inferred by the pRT retrieval. The dashed line indicates the emission contribution function averaged across wavelength. Most of the flux is emitted between 0.01 and 0.03 bar, just above the location of the silicate cloud layer whose optical depth is indicated by the purple shading. Also shown are representative condensation curves for $MgSiO_3$, Mg_2SiO_4 and Fe, all of which are expected to condense deeper in the atmosphere than what is found by the retrieval. Right panel: the best-fit ExoRem forward model and the maximum-likelihood model from the pRT retrieval are compared to the observed spectrum of YSES-1 c.

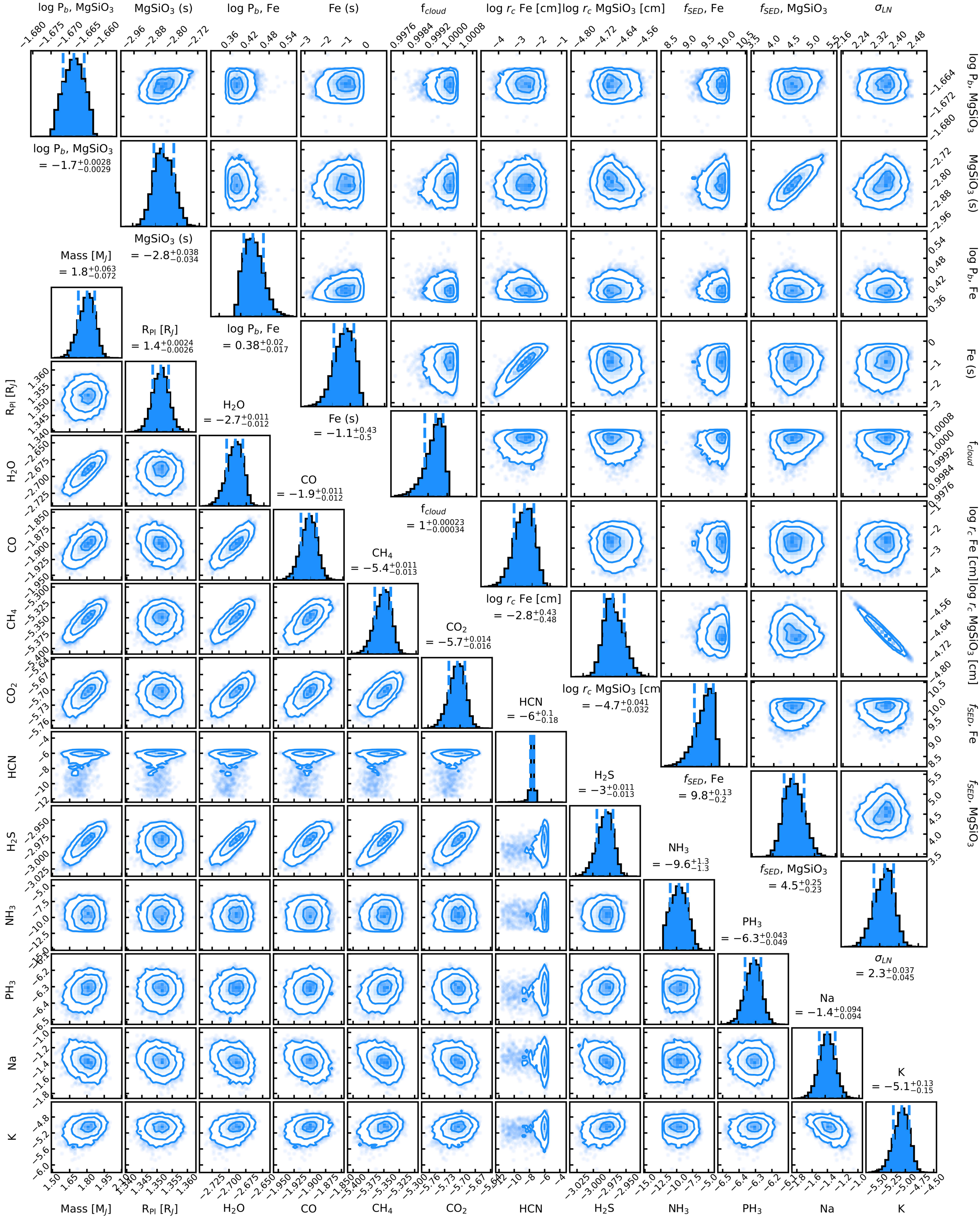

Extended Data Fig. 5 | Posterior parameter distributions for YSES-1 c as inferred from the pRT retrieval. Not shown are the parameters for the PT profile, which is shown in Extended Data Fig. 4. The units of the chemical abundances are in log mass fraction.

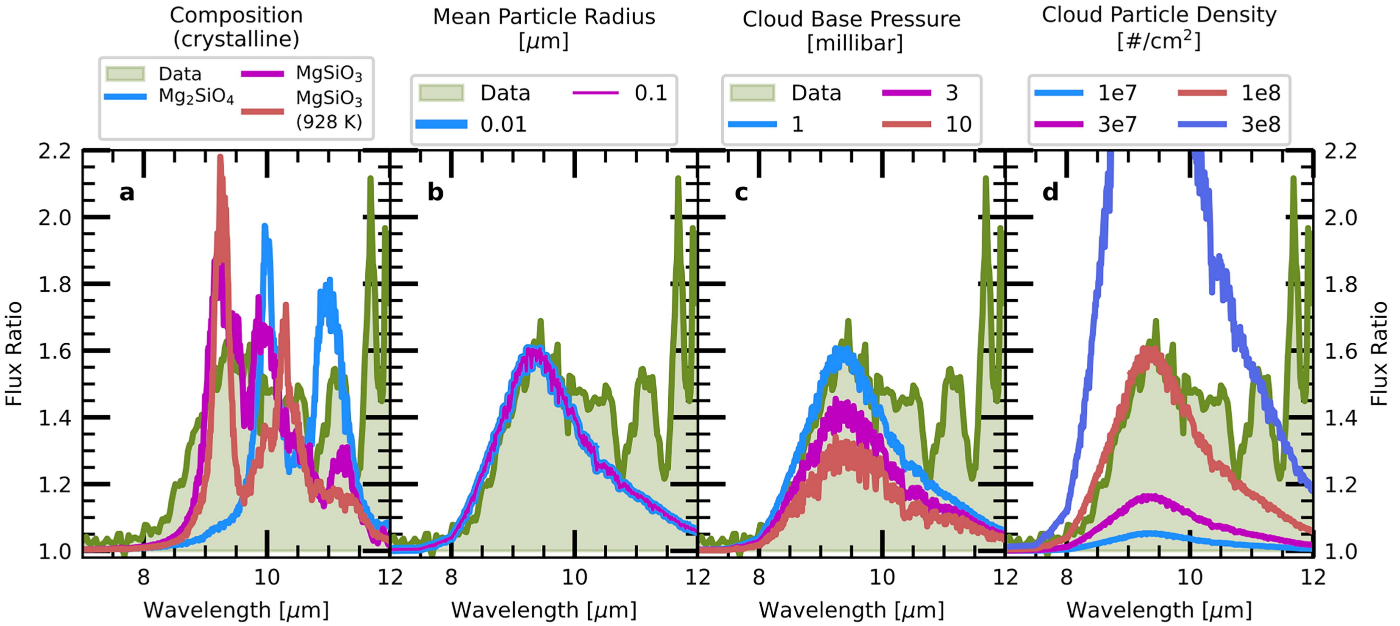

Extended Data Fig. 6 | Cloud composition, mean particle radius, cloud base pressure, and cloud particle density fits. Shown in panel 1 are different silicate species of crystalline Mg_2SiO_4, crystalline $MgSiO_3$ (averaged over all temperatures), and crystalline $MgSiO_3$ at 928 K; panel 2 shows different particle radii fits; panel 3 shows different cloud base pressures; and panel 4 shows different particle densities, all against YSES-1 c.

Extended Data Table 1 | Overview of JWST observations

Target(s)	Instrument and mode	Date	Dithers/Nods	N. Groups	Total Exposure Time (s)	Description
YSES-1 b & c	NIRSpec Prism IFU	6/19/2023	4	17	1050*	Both companions in FOV
YSES-1 b	MIRI LRS	4/25/2023	2	90	500	YSES-1 b in slit
YSES-1 c	MIRI LRS	4/25/2023	2	300	5000	YSES-1 c in slit

*Only half of the total NIRSpec exposure time was used for analyses as noted in the text.

Extended Data Table 2 | Priors for ExoREM forward model fitting and petitRADTRANS retrieval fitting

Parameter	Prior
ExoREM FM	
T_{eff} [K]	U(400, 2000)
log(g) [dex]	U(3.0, 5.0)
[M/H]	U(-0.5, 0.5)
C/O	U(0.1, 0.8)
T_{disk} [K]	U(1, 1000)
R_{disk} [R_J]	U(0, 100)
pRT Free Retrievals	
Mass [M_J]	U(0.5,12)
Radius [R_J]	U(0.7,3.0)
T_{bottom} [K]	U(2000,12000)
$dlnP/dlnT_1$	N(0.25,0.025)
$dlnP/dlnT_2$	N(0.25,0.045)
$dlnP/dlnT_3$	N(0.26,0.05)
$dlnP/dlnT_4$	N(0.20,0.05)
$dlnP/dlnT_5$	N(0.12,0.045)
$dlnP/dlnT_6$	N(0.07,0.07)
$dlnP/dlnT_7$	N(0.0,0.1)
$dlnP/dlnT_8$	N(0.0,0.1)
$dlnP/dlnT_9$	N(0.0,0.1)
$dlnP/dlnT_{10}$	N(0.0,0.1)
σ_{LN}	U(1.05,3.0)
log(K_{zz}) [log cm^2 s^{-1}]	U(3.0,13.0)
$f_{SED,X}$	U(0.0,10.0)
log(r_{cloud}) [cm]	U(-7.0,10.0)
f_{cloud}	U(0,1)
log(P_{cloud}) [bar]	U(-6,3)
log(X_i)	U(-12,-0.3)
b	U(-40,-20)
pRT CPD	
T_{disk} [K]	U(10,1000)
R_{disk} [R_J]	U(1,100)

*U(a,b) is a uniform prior in the interval a,b, while N(μ,σ) is a Gaussian prior with mean μ and standard deviation σ. For the pRT retrieval, the parameters are as described in ref. 50.

Extended Data Table 3 | Summary of forward modelling, retrieval fitting, and thermal modelling

Model	T_{eff} [K]	log g [cm s^{-2}]	[M/H]	C/O	R_{pl} [R$_J$]	T_{disk} [K]	R_{disk} [R$_J$]	Wavelength range [µm]	nParam	DoF	χ^2/ν
YSES-1 c											
FM with ExoREM only	958-10+20	3.63-0.06+0.07	0.27-0.08+0.11	0.61-0.01+0.01	1.48-0.04+0.05	N/A	N/A	< 7.5	7	N/A	N/A
FM with ExoREM + Blackbody	984-17+29	3.69-0.13+0.19	0.34-0.10+0.08	0.61-0.05+0.03	1.41-0.05+0.05	49-35+38	37-24+32	0.6-14.0	9	N/A	N/A
pRT Retrieval	1025 ± 1	3.41 ± 0.02	0.52 ± 0.01	0.798 ±0.003	1.351 ± 0.003	N/A	N/A	0.88-12.0	35	1086	7.18
Inflated Retrieval	1095.0± 1.5	3.05± 0.02	0.06± 0.03	0.723 ±0.008	1.161 ± 0.003	N/A	N/A	0.88-12.0	37	1088	0.93
Adopted range	950–1100	3.0–3.7	0.030–0.38	0.60–0.72	1.2–1.5	N/A	N/A	N/A	N/A	N/A	N/A
YSES-1b											
FM with ExoREM only	1513-25+36	4.63-0.24+0.23	-0.01-0.17+0.19	0.59-0.10+0..15	3.38-0.15+0.12	N/A	N/A	0.6-14.0	7	N/A	N/A
FM with ExoREM + Blackbody	1607-22+24	4.56-0.41+0.26	0.20-0.20+0.15	0.70-0.08+0.05	2.97-0.09+0.08	371-53+46	7.35-1.74+2.75	0.6-14.0	9	N/A	N/A
Inflated Retrieval	2002-9+13	2.9-0.1+0.2	N/A	N/A	1.82±0.02	515.0 ± 4.0	17.5±0.2	0.6-12.0	40	1051	1.03
Adopted range	1600–2020	2.8–4.8	0.00–0.35	0.62–0.75	1.8–3.1	320–520	5.6–18	N/A	N/A	N/A	N/A
Thermal IR	N/A	N/A	N/A	N/A	N/A	602.1-56+36	10.5 ± 1.7	> 7.5	5	320	0.014